Received: August 29, 2023. Revised: October 4, 2023.

INASS

International Journal of
Intelligent Engineering & Systems

http://www.inass.org/

Guided Co-operative Waderhunt Neural Network for Measuring the Temperature of Visible Heat Source

Sanket Satish Mane[1] **Ajit Kumar Santra[2]***

[1]*School of Electronics Engineering, VIT Vellore, Tamil Nadu, India*
[2]*School of Computer Science Engineering and Information Systems, VIT Vellore, India*
* Corresponding author's Email: ajitkumar@vit.ac.in

Abstract: In this article, a novel optimization-assisted deep learning (OptiA-DL) strategy is proposed to effectively measure the temperature of visible heat sources. Initially, the image is acquired from the heat source and filtered using gelatin paper. The guided co-operative trilateral filter (GCTF) is used for image smoothening and HSV (Hue, Saturation, Value) or RGB (Red, Green, Blue) structure for colour transformation. Then, an improved Gaussian mixture model (IG-MM) is applied to segment the image into various portions. Accordingly, the compact split attention-based convolutional waderhunt autoencoder network (CSAtt-CWAN) is used for temperature prediction. In CSAtt-CWAN, the parameters are tuned using the waderhunt optimization algorithm (WHOA). The proposed OptiA-DL strategy is implemented in the Python platform through the candle flame dataset and assessed the performance in terms of different evaluation measures. Moreover, a proposed OptiA-DL's performance is compared with existing methods to determine its efficiency in temperature measurement. The minimum mean square error (MSE) value obtained by the proposed OptiA-DL strategy is 0.076, which is lower than the existing methods for measuring the temperature of the visible heat source.

Keywords: Visible heat source, Gelatin filter, Improved gaussian mixture, Guided co-operative trilateral filter, Optimized deep learning, Compact split attention, Waderhunt optimization, Temperature measurement.

1. Introduction

Typically, the second most frequently measured physical quantity after time is deliberated temperature. In the industrial world, temperature provides important information as it serves as an indicator of the condition of machine parts and other production products [1-3]. The measurement of temperature is a crucial requirement in all industrial processes. Presently, instruments and methods for measuring the temperature of various heat sources encompass thermocouples, contact type sensors, pyrometers, etc. The pyrometers fall into the non-contact temperature measurement category and are only used to measure the temperature at specific, targeted locations. It is a highly risky and difficult task to detect the temperature of visible sources of heat, such as incandescent lamps, furnaces, burners, boilers, etc., with the support of sensors [4]. In addition, the installation of conventional sensors like resistance temperature detectors (RTD) close to high-temperature heat sources is remarkably challenging [5, 6].

In industry, conventional sensors are mainly employed to monitor the temperature of heat sources. These typical sensors fail while fast temperature readings are desired, such as during welding, because they cannot accurately measure quickly. Thermocouples are employed to determine the temperature at specific points, such as hot spots in boilers, ovens, furnaces, and other heat sources. At higher temperatures, thermocouples can only be used two or three times before they fail, necessitating periodic thermocouple replacement due to their breakage [7, 8]. Hence, it is necessary to turn off the entire unit in order to replace a thermocouple within a furnace or boiler. Due to its complexity and time consumption, the shutdown process affects the

system's efficiency and is followed by process maintenance. The surface area of the furnace is scanned using an optical pyrometer to determine its overall temperature distribution. However, it is not recommended to leave the boiler or oven door open for a long period of time [9, 10].

Therefore, a system that offers non-contact temperature estimation as well as may deliver point source temperature and temperature distribution must be designed to be more accurate, efficient, reliable and cost-effective [11, 12]. Furthermore, RGB and HSV colour models are used to characterize the methane flame's colour spectrum under varied burning conditions rather than resolving the actual physical spectrum. Digital image processing is used to designate the colors of different diffusion and premixed methane flames. The findings show that each kind of flame has a distinctive distribution in the HSV and RGB colour spaces [13, 14]. For the purpose of measuring the temperature of the combustion flame, an amalgamation of two-color radiation thermometry and image-processing methods is provided.

Moreover, using an optical beam splitter and a charge-coupled device (CCD) camera [15, 16] is discussed to measure the temperature of a pulverized coal flame. The methods designated so far depend on spectral distribution and pyrometry. Thus, there is no doubt that analogue processing methods are used for the measurements. In recent years, machine learning (ML) techniques have been effectively used to estimate temperature with less information. These techniques can capture complex relationships between output and input data, making them powerful tools in various fields. Various models have been assessed, such as random forest (RF), support vector machine (SVM), artificial neural network (ANN), and so on [17, 18].

Nevertheless, there is still a gap in the efficiency of these approaches. Compared to traditional ML techniques, deep learning (DL) methods [19, 20] are more suitable for dealing with various applications. In addition, DL methods can automatically learn feature representations from raw data and then generate outputs. They operate in an end-to-end manner and are practical as well as achieved promising results in many application areas like natural language processing, computer vision, speech recognition etc. The primary benefit of DL techniques is that they do not necessitate an explicit feature extraction phase by human experts. Instead, DL models execute feature extraction automatically and implicitly depending on their strong data learning abilities and adjustable processing designs.

Motivation: Flame temperature measurement has always been a significant research area in the combustion field, for instance, the temperature can replicate the burning state and judge, and analyze the flame. Accurate estimation of temperature from the heat source is vital to change the ignition model, enhance the combustion system and regulate pollution emissions. Recently, with the advancement of digital imaging technology, radiation thermometry that depends on color CCD has turned into a hot topic in the research field of temperature estimation. It is generally utilized in national defense research, scientific research and industrial production. Several works have focused on improving the estimation accuracy as well as the scope of the image temperature estimation process. Regardless of greater efforts to further enhance the temperature estimation accuracy, the error that occurred through underexposure and overexposure of image pixels has not yet been solved. The proposed study focused on introducing a novel image temperature measurement strategy using the DL method. The proposed study collects flame images from visible heat sources using the camera and divides them into different segments after processing. Finally, it provides a more accurate temperature prediction with minimum error measurements.

Contribution: The major contribution of the proposed study of temperature measurement from visible heat sources is specified below as follows:

- To introduce a novel optimization-assisted deep learning (OptiA-DL) strategy for measuring the temperature of visible heat sources.
- To offer a guided co-operative trilateral filter (GCTF) for eliminating the reflection and smoothening the flame images.
- To present an image segmentation approach using an improved Gaussian mixture model (IG-MM) for dividing the image into various portions. Here, the Kepler optimization algorithm (KoA) is applied to determine the parameters of IG-MM.
- A combined compact split attention-based convolutional waderhunt autoencoder network (CSAtt-CWAN) is provided as a classifier to offer accurate parameter measurement. The waderhunt optimization algorithm (WHOA) is adapted in CSAtt-CWAN to tune the hyperparameter by minimizing loss.
- The proposed OptiA-DL strategy attains

greater performance measures in the assessment phase as well as demonstrates promising outcomes and has the ability to be applied in industrial sectors for temperature measurements.

The remaining structure of the paper is specified as follows: Section 2 discusses the related works. Section 3 deliberates the proposed methodology for temperature measurement. Section 4 conveys the result and discussion. Finally, Section 5 exemplifies the conclusion and future scope.

2. Related works

Mehmet Cem Catalbas & Matej Bernard Kobav [21] suggested an evaluation of correlated colour temperature (CCT) using a deep regression model from RGB images. Owing to the deep regression model, CCT values for the surroundings were estimated nearer to the results of the spectroradiometer measurement. To create a regression model, a DL network structure was trained on 191 different, custom-made RGB images and their associated CCT values. Using diverse real-scene test images, the performance of this approach was compared to alternative CCT calculating methods. Even with improved performance, the error rate was higher.

In order to estimate temperature based on a color-temperature correlation model, Goutam Agrawal et al. [22] suggested a flame temperature prediction model based on ML strategy. The colour of the flame was determined by pre-processing the input image using histogram back-projection. Both SVM and ANN had employed and compared to determine the temperature. The RGB pixel of the output image was separately given to SVM and ANN in order to estimate the temperature. According to simulation data, SVM outperforms ANN however, this method had revealed maximum mean absolute error (MAE) and mean squared error (MSE).

Shinya Sawada et al. [23] provided time-series temperature measurements using magnified two-color pyrometry through blue-backlit imaging during the combustion of coal char from a single coal dust particle and volatiles. A steep temperature gradient was created by adding pulverized coal particles to a high temperature zone created by air diffusion or countercurrent hydrogen flame. Two-color pyrometry and high-speed magnified imaging were used to determine the time-series temperature of a single pulverized coal particle surface combustion and volatile matter combustion. The outcomes showed that char combustion and volatile matter were influenced by particle size. The drawback of this measurement includes less accuracy and more error rate.

The temperature measuring scheme of flame image fusion based on various exposures was presented by Liang Shan et al. [24]. The initial step in this scheme was to capture some images of flame radiation taken at various exposures. After that, segmentation was employed to identify the areas of each radiation image with a favorable exposure effect. An experimental system had constructed to adjust the temperature estimation parameters through a blackbody furnace and two-color pyrometry. A candle flame was chosen as the object of estimation, and an accurate and complete flame temperature distribution was obtained. However, this scheme is required to improve the performance of flame temperature distribution.

Weijie Yan et al. [25] introduced a technique to readjust the two-distribution distribution of volume and temperature concentration from color images. The particle volume concentration field and the temperature field of a non-uniform sediment flame were reconstructed simultaneously using a mathematical simulation based on a wide response range of a color CCD camera without incorporating monochromatic filters. The effects of camera position point errors, measurement noise, number of cameras and different reconstruction processes on the measurement accuracy were examined. Higher error rates and less accuracy were the shortcomings of this technique.

Problem statement: Recently, there have been several methods of measuring temperature as it plays an important role from industry to household. Some authors had measured the temperature using soft computing based on computer vision from a visible heat source. The contact-free temperature estimation model, ANN, infrared method, image-based combustion, and flame detection are lately suggested to improve temperature measurement. Also, temperature prediction is possible using image processing and photography. Although various methods have been introduced and are now widely used in practice, there are still erroneous temperature measurements, complicated calibration processes, and high costs. However, due to the advancement of DL in various applications, a new method based on DL strategy is necessary in order to resolve the existing challenges.

3. Proposed methodology

The section discusses a novel optimization-

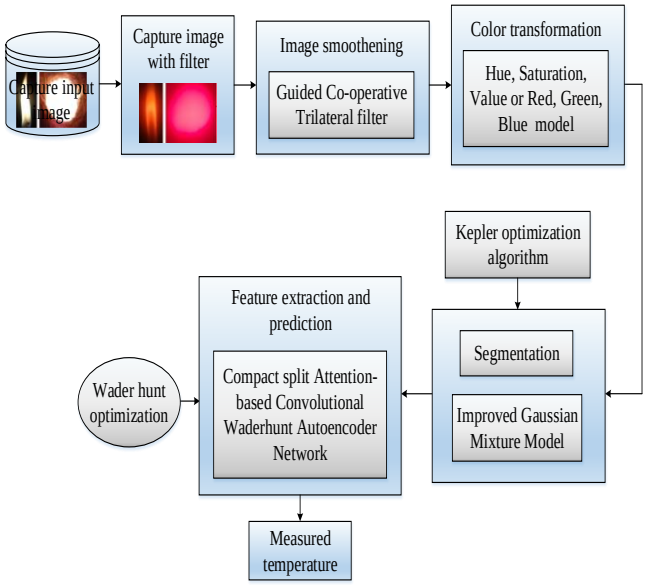

Figure. 1 Block diagram of the proposed OptiA-DL strategy

Table 1. List of notations with their description

Notations	Description
ϖ_q	Normalization term
β	Weight factor for balancing the color
χ	Weight factor for balancing depth information
ρ_t	Gaussian kernel size in spatial domain
J_{dq}	Density value in color images
J_{eq}	Depth image
P	Mixed weight
X	Encoded embedding in latent space
δ	Image in spatial space
R	Total samples
H	Color instance ranging from 0 to 365 degrees
S	Color vitality ranging from 0 to 360 degrees
V	Brightness/intensity of color

assisted deep learning (OptiA-DL) strategy to determine the temperature of visible heat sources. The proposed system encompasses different stages such as image acquisition, image pre-processing, image segmentation, feature extraction, and temperature measurement. In order to capture the images of the heat source, the proposed study utilizes a digital still camera (DSC-S60) camera. The actual temperature can be measured using a thermocouple. The next phase is pre-processing the acquired image using gelatin paper and introducing the guided co-operative trilateral filter (GCTF) for smoothening and HSV (hue, saturation, value) or red, green, blue (RGB) structure for colour transformation. After pre-processing, image segmentation is performed using an improved Gaussian mixture model (IG-MM). The block diagram of the proposed OptiA-DL strategy is presented in Fig. 1.

The image can be divided into various portions based on temperature similarity during segmentation. After that, the temperature is allocated to the available segments using colour dominance approach. Subsequently, the compact split attention-based convolutional waderhunt autoencoder network (CSAtt-CWAN) is chosen as a classifier since it provides high accuracy and is mostly utilized for non-linearity detection. Thus, by employing the proposed OptiA-DL strategy, the temperature can be efficiently predicted from visible heat sources. The list of notations of proposed Opti-DL model with their description is provided in Table 1.

3.1 Pre-processing

The images of visible heat sources, furnaces, wax candles etc., are acquired with the support of a camera. The images as well as their respective temperature, can be recorded and utilized as a database to process further. In the proposed OptiA-DL strategy, the guided co-operative trilateral filter (GCTF) is introduced for smoothening and HSV (Hue, Saturation, Value) or Red, Green, Blue (RGB) structure for colour transformation. Supposing that the color images can offer more abundant texture information, a GCTF is utilized depending on bilateral filtering. Here, the color images have been employed as guided images for smoothing the input images. The smoothening model of GCTF is specified below as follows:

$$GCFT[J]_q = \frac{1}{\varpi_q}\sum_{r\in t} H_{\rho_t}(\|q - r\|)\left(\beta H_{\rho_{sd}}(|J_{dq} - J_{dr}|) + \chi H_{\rho_{se}}(|J_{eq} - J_{er}|)\right)J_r \quad (1)$$

Where, ϖ_q indicates the normalization term, which confirms the sum of the weights as 1. β and χ signify the two weight factors employed for balancing the color and depth information. Further, the filter kernel ϖ_q has been specified as follows:

$$\varpi_q = \sum_{r\in t} H_{\rho_t}(\|q - r\|)\left(\beta H_{\rho_{sd}}(|J_{dq} - J_{dr}|) + \chi H_{\rho_{se}}(|J_{eq} - J_{er}|)\right) \quad (2)$$

Separately, each component is signified as:

$$H_{\rho_t}(\|q - r\|) = \frac{1}{2\pi\rho_t^2} exp\left(-\frac{\|q-r\|^2}{2\rho_t^2}\right) \quad (3)$$

$$H=\begin{cases}0+\frac{43\times|Gr-Bl|}{Maxi(Re,Gr,Bl)-Mini(Re,Gr,Bl)}, Maxi(Re,G\,r,Bl)=Re\\ 85+\frac{43\times|Bl-Re\,|}{Maxi(Re,Gr,Bl)-Mini(Re,Gr,Bl)}, Maxi(Re,G\,r,Bl)=Ge\\ 1710+\frac{43\times|\,Re-Gr|}{Maxi(Re,Gr,Bl)-Mini(Re,Gr,Bl)}, Maxi(Re,G\,r,Bl)=Bl\end{cases} \quad (6)$$

$$H_{\rho_{sd}}(|J_{dq}-J_{dr}|)=\frac{1}{2\pi\rho_{sd}^2}exp\left(-\frac{|J_{dq}-J_{dr}|^2}{2\rho_{sd}^2}\right) \quad (4)$$

$$H_{\rho_{se}}(|J_{eq}-J_{er}|)=\frac{1}{2\pi\rho_{se}^2}exp\left(-\frac{|J_{eq}-J_{er}|^2}{2\rho_{se}^2}\right) \quad (5)$$

Where, $\|q-r\|$ resembles the distance between q and r. J_{dq} indicates the value of density in color images and J_{eq} specify the depth image, considerably. ρ_t resembles the Gaussian kernel size in the spatial domain, which assess the smoothing level. ρ_{sd} and ρ_{se} indicate the Gaussian kernel sizes in the photometric similarity of color and depth image. Moreover, ρ_{se} contributes more abundant structural information and ρ_{sd} denotes the outcomes with more texture information.

In addition, the RGB colour space must be converted into other domains with the lowest correlation between the colour components. In order to prevent colour distortion, the HSV conversion is carried out using RGB, in which the color instance ranging from 0 to 365 degrees is given as Hue (H), the color vitality ranging from 0 to 360 degrees is specified as saturation (S) and brightness/intensity of color has resembled as value (V) . Hue is characterized by each colour angle in the cone with regard to the 0-degree line. The distance of the colour from the cone's centre signifies saturation. The vertical position of color within the cone serves as a value representation. Since a change in a single component exhibits the least impact on others, the HSV colour space delivers greater colour conversion and minimizes colour shifting. The value and saturation components are subjected to the various enhancement approaches, whereas the Hue is left unchanged. The HSV color transformation structure has been determined using the following equations.

$$S=255\times\left\{\frac{Maxi(Re,Gr,Bl)-Mini(Re,Gr,Bl)}{Maxi(Re,Gr,Bl)}\right. \quad (7)$$

$$V=255\times Maxi(Re,G\,r,Bl) \quad (8)$$

3.2 Improved Gaussian mixture model

After obtaining the smoothed pre-processed image, it is segmented into various areas based on used improved Gaussian mixture model (IG-MM). A form of density model segmentation is known as IG-MM. IG-MM comprises of Gaussian function with various weights to establish multi-model density. By allowing the approximation of complicated densities, the IG-MM technique relaxes the constraints for segmentation. IG-MM employs an unsupervised learning model to divide the input into various clusters. Each cluster of information is approximated using a Gaussian distribution, with its covariance and mean called the mixture component. IG-MM then delivers a probabilistic model for complicated densities through the superposition of Gaussian distributions. For segmentation, the image features have been distributed as follows:

$$q(y|\kappa)=\sum_{j=1}^{P}x_j h(y|v_j,\rho_j) \quad (9)$$

Where, P signifies one of the Gaussian distributions $x_j, j=1$, y indicates the continuous vector of D -dimensional image attribute, as well as P denotes the mixed weight, as provided in the below equation.

$$\sum_{j=1}^{P}x_j=1 \quad (10)$$

Because there are two issues with image segmentation, each pixel point category was determined. The image to be segmented has been described as $Z=(z_1,z_2,..,z_p)$, where z_p resembles the RGB value of each pixel. The pixel points are set to $Y=(y_1,y_2,..,y_p)$, where $y_p\in M.M$ resembles the two-dimensional vector (0,1). A set label of the class Y^* is defined, conferring to maximum a posteriori (MAP).

$$Y^*=argmax\{Q(Z|Y,\Theta)Q(Y)\} \quad (11)$$

Previous probabilities of utilizing Gibbs distribution can be specified below equation:

$$Q(Z|Y,\Theta)=\prod Q(z_j|y_j,\phi y_j) \quad (12)$$

Where, $Q(z_j|y_j,\phi)$ denotes the Gaussian distribution with parameters $\phi=(\nu,\sigma)$. In the Markov problem field, the parameter $\Theta=\{\phi_m|m\in M\}$ determined from prior knowledge.

Moreover, the parameters of IG-MM is

determined using a new physics-based metaheuristic algorithm known as the Kepler optimization algorithm (KoA). In order to determine the velocity and location of planets (parameters) at any given time, KoA imitates Kepler's law of planetary motion. Each planet in KoA serves as a candidate solution with respect to the best-so-far solution (the Sun), which is updated at random during the optimization process. The planets (candidate solutions) show different situations from the Sun at different times, allowing KoA to explore and use the search area more efficiently. The other planets get closer to the sun several times, which allows the algorithm to work more accurately as it searches for the optimal solution in new locations.

Sometimes they move so far from the sun that it is possible to more effectively search the entire search space. The distance between the sun and each planet is determined for implementation and establish the new circumstances for the selected planets using the below expression.

$$Y_{k,New}(u+1) = Y_{Best}(u) + S_{j,Best} \times V(-2,2) \quad (13)$$

The best solution (Sun) has the ability to change its location according to the Sun's movement in space, allowing for more exploration and preventing local optimums. The position change can be mathematically formulated as follows:

$$Y_{Best,New}(u+1) = Y_{Best}(u) \times V(-2,2) \quad (14)$$

In the above equations, $V(-2,2)$ offers a pseudo-random number with a uniform distribution in the range [-2,2]. In $Y_{k,New}(u+1)$, $S_{j,Best} \times V(-2,2)$ creates a new distance from the optimum solution for each solution. If $V(-2,2)$ delivers a number close to 1, the algorithm exploits; otherwise, it is explored. Due to elitism, the nearest location of the sun and the chosen planets can be calculated as follows.

$$Y_j(u+1) = \begin{cases} Y_{j,New}(u+1) if fit(Y_{j,New}) < fit(Y_j) \\ Y_j(u) Otherwise \end{cases} \quad (15)$$

Then, after performing the segmentation process, the temperature is assigned to the available segments using the color dominance approach. Color zones were established depending on the color dominance in certain areas. Each zone has different temperatures.

3.3 CSAtt-CWAN model

In this section, a compact split attention-based convolutional waderhunt autoencoder network (CSAtt-CWAN) model is employed to estimate the correlation of color temperature. Here, the CSAtt-CWAN is employed to make the database of acquired images as well as the estimated temperature for approximate temperature measurement. The training data is considered as the pixel intensity on the image and the actual temperature estimated. As soon as the training has ended on the dataset, the CSAtt-CWAN is ready to be utilized on the image, where the pixel intensity has been estimated, and temperature is measured. The CSAtt-CWAN combines different modules, such as the compact split attention (CSAtt) module and the convolution autoencoder (Conv-AE) module. The architecture of the CSAtt-CWAN model is given in Fig. 2.

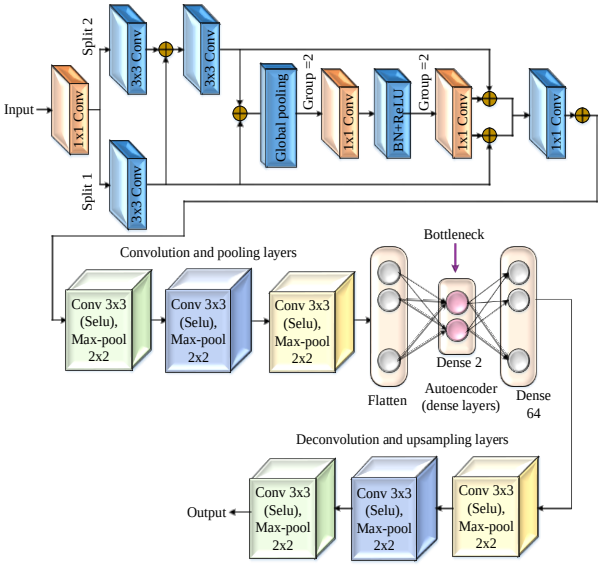

Figure. 2 Architecture of CSAtt-CWAN model

3.3.1 Compact split attention module

Here, a compact split-attention architecture is discussed initially. Large channel shared groups are used by the deep network architecture for feature extraction, which is more effective for common computer vision problems with expensive parameters and enough data. Moreover, each group in this model employs identical convolutional operations with the same receptive field size. CSAtt module retains two feature group ($P = 2$) to optimize the structure and improve its suitability while lowering the total number of parameters in the whole network. These two groups separated from the input features can undergo several transformations G_j. In both of the two groupings, one 1×1 convolution is followed using a single 3×3 convolution. The output feature maps of the other group (G_2) can sum the outcomes of the first group (G_1) and undergo another $3 \times$

3convolution for improving the representation across channels. In this way, information can be obtained from both split groups, and the reception area of the network can be extended. Therefore, the Co-SA module provides a stronger ability to extract local and global information from feature maps. The fusion feature maps are mathematically stated as follows:

$$\hat{V} = \sum_{j=1}^{P} G_j(Y_j), \hat{V} \in \boldsymbol{R}^{I \times X \times D} \quad (16)$$

Where, I, X and D imply the scales of output feature maps. The global spatial information is collected by channel-wise statistics constructed by global average pooling. It is formed by compressing transformation outcome over spatial dimensions and the d^{th} component designed by:

$$T_d = \frac{1}{I \times X} \sum_{\beta=1}^{I} \sum_{\chi=1}^{X} \hat{V}_d(\beta, \chi), T \in \boldsymbol{R}^D \quad (17)$$

A split weighted combination can capture significant information in feature maps, hence channel-wise soft attention is utilized to aggregate a weighted fusion represented by a cardinal group representation. Further, the d^{th} channel of feature maps can be determined as:

$$W_d = \sum_{j=1}^{P} b_j(d) G_j(Y_j) \quad (18)$$

Here, b_j resembles the (soft) assignment weight that can be computed as:

$$b_j(d) = \frac{exp(H_j^d(T))}{\sum_{j=1}^{P} exp(H_k^d(T))} \quad (19)$$

Where, H_j^d is quantified by utilizing two 1×1 convolutions with ReLU activation and BatchNorm, it represents the weight of global spatial information T to the d^{th} channel. Consequently, the entire CSAtt model is modelled with an ordinary residual structure that the outcome Z is computed utilizing the skip connection: $Z = W + Y$, while the output feature maps' shape is similar to the input feature maps. Else, an additional transformation U can be employed on skip connection to obtain the identical shape. For example, U can be the convolution with stride or the combination of pooling and convolution.

3.3.2 Convolutional autoencoder module

Autoencoder (AE) is primarily deliberated as the association of two neural networks, specifically the encoder and decoder. The encoder's operation is to characterize the information in limited parameters and small dimensions. The actual destination (input) is then decoded by the decoder using the encoded data. In order to extract features more effectively utilizing spatial information, convolutional neural networks are used.

Encoder: The convolution layers are fixed in the encoder for effective feature extraction. The features are then compressed into a low-dimensional space using a non-linear transformation. In such a way, the actual high-dimensional input information is effectively converted into low-dimensional information.

$$\Psi: \delta \to X \quad (20)$$

Where, Ψ resembles the encoder architecture, X specifies the encoded embedding in latent space and δ indicate the image in spatial space. The arrow between δ and X implies the encoding from spatial space to latent space.

Decoder: Here, the convolution and dense layers of the decoder utilize the encoder's output as an input for rebuilding the target. The operation of the decoder is to convert the low-dimensional representation into the high-dimensional actual data.

$$\Omega: X \to \delta \quad (21)$$

Where, Ω resembles the decoder. In the decoder stage, the embedding in latent space is mapped with intensity pixel values in spatial pace.

As mentioned earlier, ConvAE combines an encoder and a decoder. The output is flattened before being fed to a dense layer to lessen dimensionality. An encoder's primary tasks are data compression and clustering to minimalize the latent space. The decoder receives the latent space data in order to estimate the input. Moreover, the input is given, and the output is compared with the measured temperature. It generates a mapping between the actual input and the measured outcome. The operation of AE is to generalize or learn the distribution of target and input data as well as reduce the difference between them. The block diagram of AE is described in Fig. 3.

The Conv-AE in the CSAtt-CWAN model comprised 11 layers, such as 4 deconvolution layers, 2 dense layers with 128 neurons, and reshape and up-sampling layers. At the end of the decoder, the dense layer is kept, and for computing the loss, a binary cross entropy has utilized. Initially, the data is encoded before being decoded by minimalizing the loss function. Convolutions and pooling in the encoder and deconvolution in the decoder are

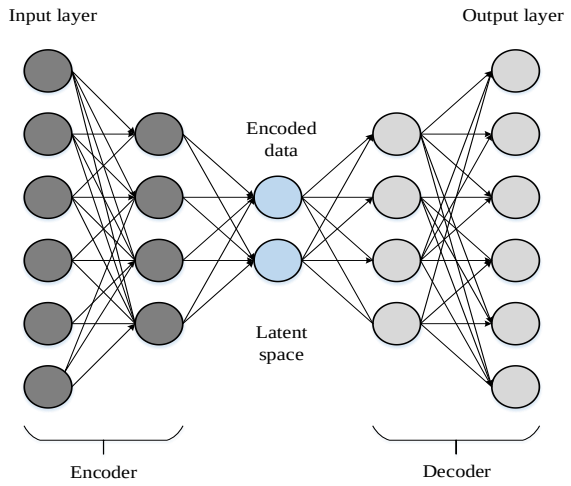

Figure. 3 Block diagram of autoencoder

implemented as part of a ConvAE. The ConvAE performs a better task of encapsulating the underlying patterns in the pixel data than the AE with fully connected layers.

$$\Omega, \psi = arq_{\Omega,\Psi} \, min \|Y - (\Omega \circ \Psi)Y\|^2 \tag{22}$$

where, $(\Omega \circ \Psi)Y$ indicates the encoding and then data decoding from spatial to latent space as well as the latent to spatial space.

This represents that $(\Omega \circ \Psi)Y$ is equivalent to Y. The loss function is deliberated as $\|Y - (\Omega \circ \Psi)Y\|^2$. The difference between $Y$and estimated output $(\Omega \circ \Psi)Y$ is minimized by optimizing the parameters of both the encoder Ψ and decoder Ω.

3.3.3 Parameter optimization using waderhunt optimization

The proposed OptiA-DL strategy has employed a waderhunt optimization algorithm (WHOA) to tune the parameters of CSAtt-CWAN. The WHOA algorithm combines the migratory behavior of the wader and the hunting behavior of the scavenger to address the optimization problems. Scavenger hunting tactics fall into four categories: finding and pursuing prey, pursuing, harassing and encircling, and attacking prey. In addition, the cohesive grouping of members improves the fitness function. The WHOA keeps the best solution (optimal parameter value) discovered during the iteration.

In addition, the scavenger's hunting behaviour helps to locate the possible location of prey. The balance between the exploitation and exploration phases is attained through the WHOA. Here, exploitation confirms that the best solution is found inside the search area. WHO's ability to reach different search spaces is ensured by exploration, which also increases the rate of convergence to achieve global convergence. The major phases involved in WHOA are encircling prey, hunting, exploitation (attacking) and exploration (searching for prey).

Encircling prey: The scavengers are quite familiar with finding and encircling prey. Here, the target prey or objective is considered for the mathematical modelling of scavengers using the current best solution. Owing to the lack of availability of search space details earlier, it is closer to the optimal solution. The positions of other search agents for the best optimal solution are updated. The mathematical equation utilized for updating, can be specified as follows:

$$\vec{B}_q = \left| \vec{C}.\vec{D}_d(j) - \vec{D}(j) \right| \tag{23}$$

$$\vec{C}(j+1) = \vec{C}_d(j) - \vec{E}.\vec{B}_q \tag{24}$$

where, $\vec{D}$ represents the position of the scavenger's, $\vec{C}_d$ resembles the position vector of prey, $\vec{B}_q$ signifies the distance between the prey and scavenger, $\vec{E}$ and $\vec{C}$ specify the coefficient vector, j indicates the current iteration. $\left| \right|$ and . indicate the absolute and multiplication value along with vectors. Further, the two dissimilar vectors $\vec{E}$ and $\vec{C}$ has been specified as,

$$\vec{C} = 2.p\vec{r}_1 \tag{25}$$

$$\vec{D} = 2\vec{q}.p\vec{r}_2 - \vec{q} \tag{26}$$

$$\vec{q} = 5 - (k * (5/Maxi_k)) \tag{27}$$

Where, k indicates the iteration that ranges between $k = 1,2,\ldots Maxi_k$.

Throughout the iteration, $\vec{q}$ has minimized linearly between 5 and 0 for maintaining the balance between the exploitation and exploration stage. $p\vec{r}_1$ and $p\vec{r}_2$ are the random vectors that range [0,1]. Besides, the scavengers randomly update the location during the prey.

Hunting: Scavengers usually live in groups and rely on a trusted friend group to help them to find their prey. The optimum scavenger behavior is based on the best search agent, who is aware of the location of the prey. The cluster's remaining members save the optimal location for updating each member's

position, and their positions are described as,

$$\vec{B}_q = \left|\vec{C}.\vec{D}_d - \vec{D}_n\right| \quad (28)$$

$$\vec{D}_n = \vec{D}_q - \vec{E}.\vec{B}_q \quad (29)$$

$$\vec{F}_q = \vec{D}_n + \vec{D}_{n+1} + \ldots + \vec{D}_{n+R} \quad (30)$$

Where, D_q implies the location of the first best scavenger, $\vec{D}_n$ states the location of other scavengers, and R denotes the total number of scavengers.

Exploitation: In the scavenger exploitation stage, the vector $\vec{q}$ is reduced. Likewise, the value of vector $\vec{E}$ is also reduced from 5 to 0 to vary $\vec{q}$ during iteration. Here, the scavengers in the group have enforced to attack the prey when the value is $|E < 1|$. Now, the equation of prey attacking can be described as,

$$\vec{D}(j+1) = \frac{\vec{F}_q}{R} \quad (31)$$

Where, the finest solution is saved in $\vec{D}(j+1)$, and it updates other search agents' locations concerning the attack position to the prey.

The location updation considering the wader's migratory characteristics is described as,

$$\vec{D}(j+1) = \vec{D}(j) + \xi\left[\left(\vec{D}_c(j) - \vec{D}_{np}(j)\right)\right] \quad (32)$$

where, $\vec{D}(j+1)$ indicates the wader location at $(j+1)^{th}$ iteration, $D(j)$ states the wader location at j^{th} iteration, $\vec{D}_c(j)$ represents the best location determined by wader at j^{th} iteration, $\vec{D}_{np}(j)$ implies the location of n^{th} wader in p^{th} direction at j^{th} iteration. ξ signifies to Gaussian random number with Rpopulation, and it can be used for improving the search area.

Moreover, the location updating is formulated through the incorporation of the wader's migratory characteristics as well as the scavenger's hunting characteristics. It can be described as:

$$\vec{D}_{New}(j+1) = 0.5[\vec{D}(j+1)_{Scavenger}] + 0.5[\vec{D}(j+1)_{Wader}] \quad (33)$$

$$\vec{D}_{New}(j+1) = 0.5\left[\frac{\vec{F}_q}{R} + [\vec{D}(j) + \xi[D_c(j) - D_{np}(j)]]\right] \quad (34)$$

Thereby, the balance between exploration and exploitation has been sustained, supporting premature convergence.

Exploration: In this stage, the scavengers look at the prey concerning the members of the group which exist in $\vec{F}_q$ vector. During prey search, each member of the group moves away and attacks the prey. Thereby, $\vec{E}$ has been employed to make the search agents look for prey using a random value greater than +1 or lower than -1 while they are moving from the prey. Thus, the behaviour of global search has improved using this search mechanism.

Re-estimation of fitness: After updating the scavenger location, the fitness can be re-estimated to identify the viability of the solution. It is described as,

$$N = \frac{1}{R}\sum_{j=1}^{R}\left(B_j - \vec{B}_j\right)^2 \quad (35)$$

Where, R resembles the total samples, $\vec{B}_j$ indicates the detected output and B_j resembles the targeted output.

Termination: These processes are repeated until the maximum number of iterations is reached, and the globally optimal solution is found. The pseudocode of WHOA is provided in Algorithm 1.

Algorithm 1: Pseudocode of WHOA for parameter tuning

Start
Initialize the number of population R
Initialize the parameters q, C, E
Compute the fitness value N
while $(j < Maximumiteration)$ do
for each scavengers (parameter), do

Update the present location using $\vec{D}_{New}(j+1) = 0.5\left[\frac{\vec{F}_q}{R} + [\vec{D}(j) + \xi[D_c(j) - D_{np}(j)]]\right]$
end for
Update q, C, E, R
Compute the fitness value N
Update the location of F_q using $\vec{F}_q = \vec{D}_n + \vec{D}_{n+1} + \ldots + \vec{D}_{n+R}$
Update the group D_q relating to F_q
$j = j + 1$
end while
Return D_q
end

Table 2. System configuration of proposed OptiA-DL strategy

Parameters	Configuration
System type	64-bit operating system, x64-based processor
Installed RAM	4.00 GB(3.83 GB unstable)
Processor	Intel® Core™ i3-3245 CPU @3.40 GHz,3.40GHz
Pen and touch	No pen or touch input is available for this display.

Table 3. Hyperparameter setup of OptiA-DL strategy

Parameters	Values
Input layer of CSAtt-CWAN	Pixel intensity values of the image is present
Output layer of CSAtt-CWAN	Provides the temperature value resultant to pixel intensity
Maximum epoch	14
Learning rate	0.01
Dropout Rate	0.5
Optimizer	WHOA
Activation function	ReLU

4. Results and discussion

In this subdivision, the results of the proposed OptiA-DL strategy are discussed for measuring the temperature of visible heat sources. The OptiA-DL strategy is simulated using Python software, and the performance is estimated in varied performance indicators. The WHOA algorithm is used for tuning the parameters. Similarly, the learning rate has been set to a default value of 0.01 in each task, and the activation function ReLU has been chosen to render the experimental results. The default dropout rate is set to 0.5, the mini-batch size is set to 10, and the epoch size is set to 14. Additionally, several existing approaches are reflected to compute and scrutinize the temperature measurement performance of the OptiA-DL strategy.

Further, the image of visible heat sources furnace, wax candle, boiler images has been taken with the use of camera. The image and their corresponding temperature has been recorded and utilized as database for processing further. For experimentation, Bunsen burner has utilized as a controlled source. The fuel/air ratio has varied by controlling the air. The Bunsen burner images are acquired in the dark room for three typical fuel/air ratio. Also, the proposed OptiA-DL strategy has utilized the candle flame images for analysis. The images are stored in JPEG format. Table 2 describes the system configuration of the OptiA-DL strategy for simulation. Table 3 signifies the hyperparameter setup of the OptiA-DL strategy.

4.1 Performance indicators

The proposed OptiA-DL strategy is trained and tested using the metrics presented in this section. These indicators support evaluating how effectively the OptiA-DL strategy has learned. The performance of the OptiA-DL strategy is assessed in this study using the mean square error (MSE), mean absolute error (MAE), and root mean square error (RMSE).

Mean square error (loss): MSE resembles the average squared difference between predicted and actual values in the dataset. It is also deliberated as MSE loss or loss. When the value of MSE is smaller, it is said that the proposed OptiA-DL strategy has improved learning.

$$\Omega_{MSE} = \frac{1}{P}\sum_{j=1}^{P}(z_j - \hat{z})^2 \quad (36)$$

Where, P represents the number of samples, z_j indicates the actual value and $\hat{z}$ resembles the predicted value.

Mean absolute error: The MAE specifies the average absolute difference between the actual and predicted values in the dataset.

$$\Omega_{MAE} = \frac{1}{P}\sum_{j=1}^{P}\left|z_j - \hat{z}\right| \quad (37)$$

Root mean square error: RMSE is generally defined as the square root of MSE and computes the standard deviation of residuals.

$$\Omega_{RMSE} = \sqrt{\Omega_{RMSE}} = \sqrt{\frac{1}{P}\sum_{j=1}^{P}(z_j - \hat{z})^2} \quad (38)$$

4.2 Performance analysis

This section provides the performance analysis of a proposed OptiA-DL strategy with the existing models. After testing the proposed OptiA-DL strategy on the candle flame dataset, the evaluation metrics are analysed and compared with other existing methods. The proposed OptiA-DL strategy utilized gelation paper as a filter and smoothed the images using GCTF. The gelatin paper is mounted in a web/mobile camera and captured the images. The normal image comprises identical pixel intensity and a lot of reflections; however, if the visible heat source

(a) (b) (c)

Figure. 4 Result of filtering using gelatin paper: (a) Input image, (b) Used gelatin paper, and (c) Filtered image

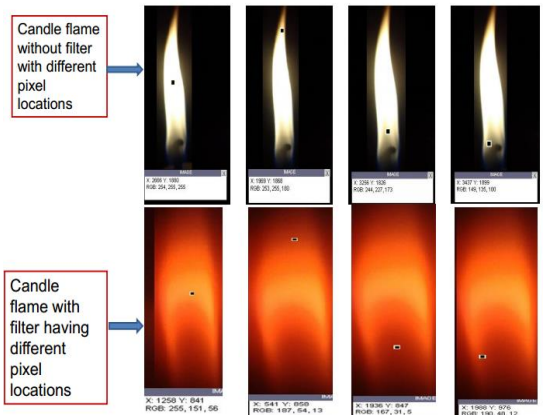

Figure. 5 Candle flame without filter and with filter for different pixel locations

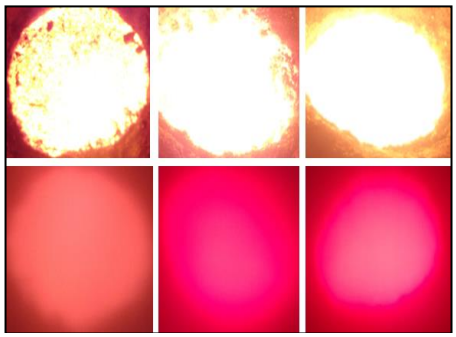

Figure. 6 Boiler images with dissimilar temperatures (Normal and filtered images)

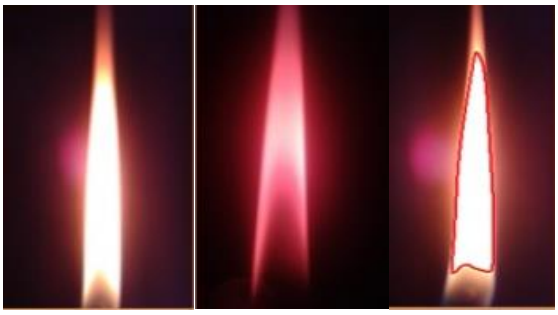

(a) (b) (c)

Figure. 7 Segmentation using IG-MM: (a) Input image, (b) Filtered image, and (c) Segmented image

image is captured from the filter, the reflections are entirely removed. In the central part of the candle flame, the pixel intensity is larger, and the intensity decreases up and down, similar to the temperature. After smoothening, the segmentation process has done using IG-MM. Fig. 4 offers a sample of the outcomes during filtering. The candle flame without filter and with filter for different pixel locations is provided in Fig. 5. In the same way, the boiler images with dissimilar temperature (Normal and filtered images) is provided in Fig. 6. Here, the boiler images have been acquired by utilizing a camera away from a distance of 4 meters. With the support of the filter, the non-linear characteristics are effectually removed. At various points in the filtered image, the pixel intensity and the resulting temperature are recorded as a database.

Table 4. Estimated temperature along with the pixel intensity for the candle flame

X	Y	Red	Green	Blue	Measured Temperature
72	854	66	11	4	217
114	886	75	15	7	255
2284	830	98	16	5	370
2117	823	133	20	4	410
1947	820	160	28	5	470
1807	834	194	44	9	537
621	865	221	71	21	580
1644	851	237	67	18	642
952	903	252	113	22	674
1147	830	255	156	55	606

As discussed earlier, temperature sensors such as thermocouples are used to measure the flame's temperature. By generating various flame sectors, the temperature is estimated. Temperature readings are taken when the sensor has moved around the flame in various positions.

The candle flame is separated into many zones, as seen in Fig. 7. The IG-MM segmentation approach permits the distinction of distinct zones and the observation of colour dominance. For the correlation of temperature and colour, the RGB/HSI model is employed. The blue, red, and intensity factors are given more consideration.

The CSAtt-CWAN is trained with the image's red component as well as its resultant temperature data. Table 4 offers the estimated temperature along with the pixel intensity.

As the temperature increases, the pixel intensity also rises, according to Table 4. It has been discovered that the RGB model works well for processing CSAtt-CWAN. The *XY* coordinates, red component value and corresponding estimated temperature are utilized as a database.

The pixel intensity analysis with respect to X-axis

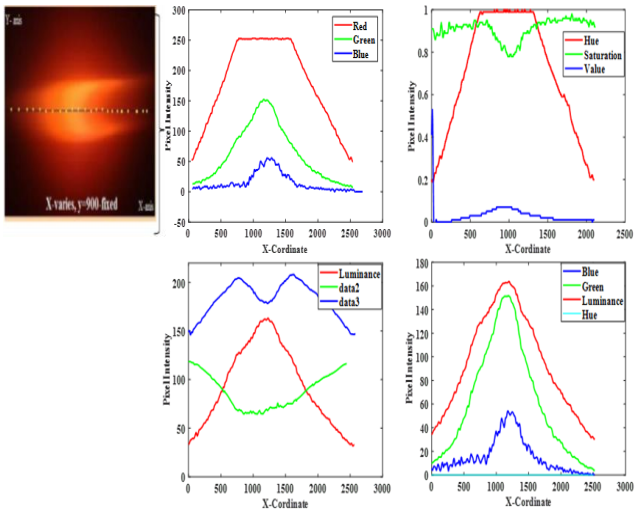

Figure. 8 Pixel intensity analysis with respect to X-axis and Y-axis fixed at y=900

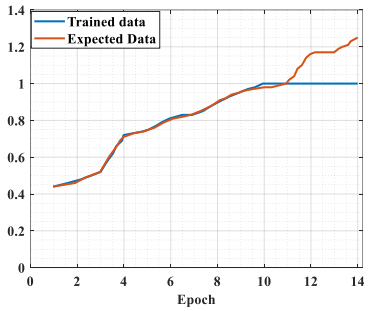

Figure. 9 Analysis of actual and trained data

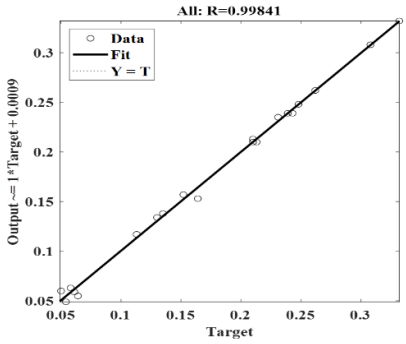

Figure. 10 Regression plot for training state

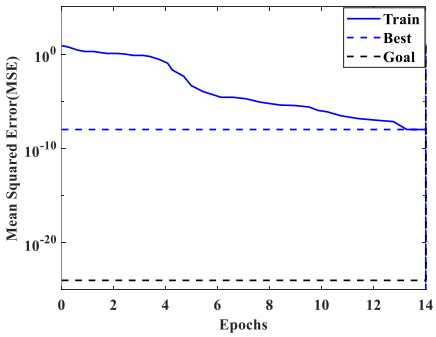

Figure. 11 MSE analysis by varying the epoch size

and Y-axis fixed at y=900 is offered in Fig. 8. Here, it is seen that the pixel intensity varies according to

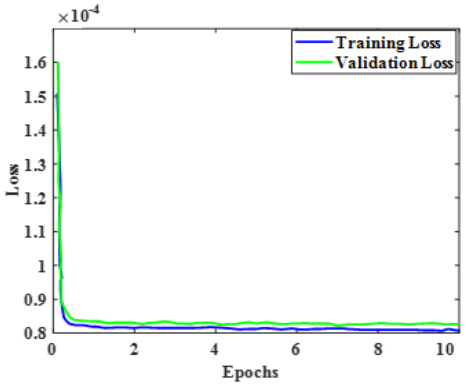

Figure. 12 Training and validation loss

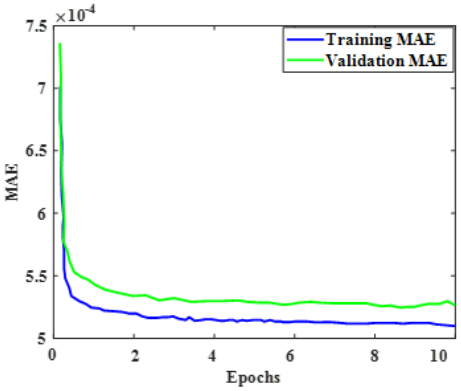

Figure. 13 Training and validation MAE

flame intensity. In RGB, the red intensity saturates in the middle. The red, blue, green, Hue and luminance components can be used to train neural network models shown in Fig. 8. The analysis between the expected and trained data is presented in Fig. 9. The training data is employed to train the network for predicting an expected outcome. Initially, the training data has employed to fit the neural network, which is provided to measure the temperature for the given input. The graphical representation analyses the expected and trained data with different epochs.

When the value of epoch size increases, the value of training expected and expected trained data is also increased.

The graph shows that the proposed OptiA-DL strategy has achieved expected values close to the trained data. Moreover, the correlation between the actual and target output is provided using a regression plot demonstrated in Fig. 10. The MSE analysis by varying the epoch size is described in Fig. 11.

The analysis of training and validation loss is presented in Fig. 12. In the graphical representation, the horizontal axis resembles the epoch unit, and the vertical axis indicates the loss function. The MSE is the loss function, and the WHOA optimized has been utilized. The graph shows that training and validation loss reduces rapidly over initial epochs. Further,

relating to the first and last epoch values, the performance of the proposed OptiA-DL strategy has enhanced during training and validation.

In the same way, the analysis of training and validation MAE is offered in Fig. 13. Here, the horizontal axis resembles the epoch unit, and the vertical axis indicates the MAE. As MAE reduces, the OptiA-DL strategy is better at measuring the temperature of visible heat sources. The graphical representation demonstrated that the proposed OptiA-DL strategy minimized the MAE value and showed that the network is becoming more accurate as it has been trained.

MSE is reflected as a significant metric that supports discovering the error measures (difference between actual and predicted value). Fig. 14 states the MSE analysis in contrast with the proposed OptiA-DL strategy and other existing models. If the value of MSE is lower, the proposed OptiA-DL strategy is deliberated as superior for temperature measurement. In addition, it is perceived that the proposed OptiA-DL strategy has better accuracy of detection owing to the minimization of the error rate. For comparison, the existing methods such as bidirectional long-short term memory (Bi-LSTM), bidirectional gated recurrent unit (Bi-GRU), artificial neural network (ANN), and convolution neural network (CNN) are considered.

In the graphical illustration, the proposed OptiA-DL strategy has achieved a minimum MAE value than existing approaches. The minimum MAE value reached by the proposed OptiA-DL strategy is about 0.076, whereas the existing approaches have gained greater MAE values of 0.182 for Bi-LSTM, 0.11 for Bi-GRU, 0.1 for ANN, and 0.082 for CNN.

Fig. 15 describes the performance of RMSE for the proposed OptiA-DL strategy and existing methods. When the value of RMSE is lower, the proposed OptiA-DL strategy is deliberated as superior. During the observation of the graphical illustration, the proposed OptiA-DL strategy has accomplished supreme RMSE values of 0.011 and is lower than the existing approaches. Moreover, by considering the input values based on CSAtt-CWAN along with IG-MM, the proposed OptiA-DL strategy has effectively measured the temperature and proved superior to the existing methods. The existing approaches, such as Bi-LSTM, Bi-GRU, ANN, and CNN, have acquired RMSE values of 0.033, 0.017, 0.018, and 0.016 which is higher than the OptiA-DL strategy since the temperature estimation is not better.

Fig. 16 validates the performance of MAE for the proposed OptiA-DL strategy and existing methods.

The proposed OptiA-DL strategy has acquired the lowest MAE compared with existing approaches

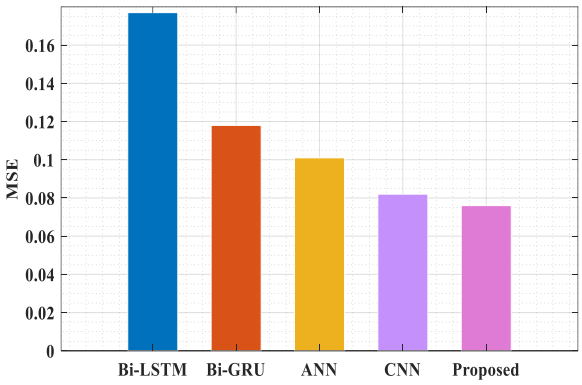

Figure. 14 MSE analysis with proposed OptiA-DL and existing methods

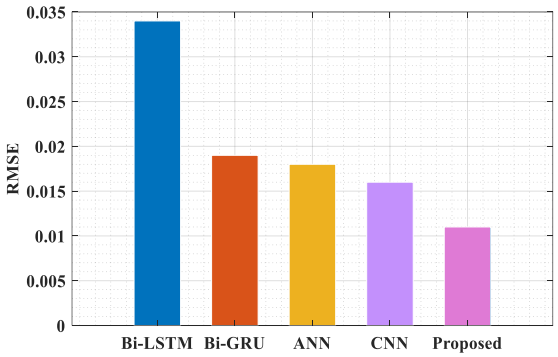

Figure. 15 RMSE analysis with proposed OptiA-DL and existing methods

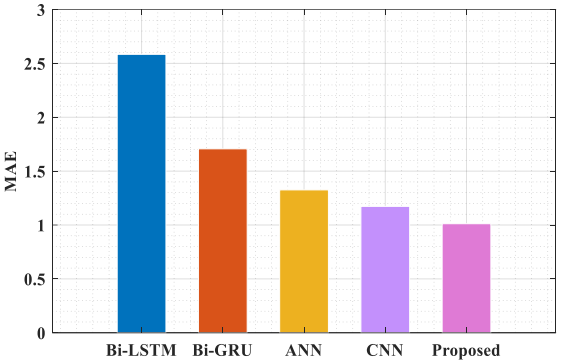

Figure. 16 MAE analysis with proposed OptiA-DL and existing methods

on account of employing the finest temperature estimation model. The existing approaches, such as Bi-LSTM, Bi-GRU, ANN, and CNN, have gained higher MAE values correspondingly. The proposed OptiA-DL strategy has obtained a minimum MAE of 1.012, which is better than the existing approaches. The existing approaches have obtained an MAE value of 2.56 for Bi-LSTM, 1.71 for Bi-GRU, 1.326 for ANN and 1.173 for CNN. Among the existing ones, Bi-LSTM has gained MAE close to the proposed OptiA-DL strategy, whereas CNN has

Table 5. Temperature measurement for proposed OptiA-DL and existing methods

Measured temperature	Predicted temperature				
	Bi-LSTM	Bi-GRU	ANN	CNN	Proposed
220	204	201	195	235	210
255	230	228	231	217	238
350	336	330	325	368	342
470	469	439	453	435	475
580	569	552	588	546	575
680	670	663	692	653	677
720	697	695	702	765	710

Table 6. Comparison of proposed OptiA-DL with state-of-the art methods in terms of MAE and RMSE

Methods	Performance metrics (%)	
	MAE	RMSE
SVM	1.707	0.019
ANN	2.584	0.034
Proposed	**1.012**	**0.011**

obtained the maximum error measure value of MAE. Accordingly, it is implicit that the OptiA-DL strategy has appropriately minimalized the rate of errors in temperature measurement due to the usage of WHOA, which minimizes the loss and reduces the error rate of neural network model for maximizing the accurate prediction of actual temperature. As a result, the overall analysis demonstrates that the estimated temperature is close to the actual temperature with the proposed OptiA-DL strategy. In addition, the temperature measurement with measured and predicted is signified in Table 5.

The tabular depiction evidently reveals the ability of the proposed OptiA-DL against existing methods.

4.3 Comparison with state-of-the art methods

Besides being assessed with different evaluation metrics, the performance of proposed OptiA-DL model has been inspected with different existing state-of-the-art methods in detail. Table 6 validates the estimated outcomes of proposed OptiA-DL and state-of-the-art methods like SVM and ANN [22].

In the tabular representation, the proposed OptiA-DL has accomplished better outcomes than the state-of-the-art methods for providing better temperature due to the ability of employed optimization that supports the CSAtt-CWAN model. To be exact, SVM arises in second place, exposing MAE of 1.707 and RMSE of 0.019, which is higher than the proposed OptiA-DL model.

4.4 Discussion

The temperature measurement is deliberated to be a significant requirement in several industrial processes. In the proposed work, the mathematical model based on OptiA-DL has been developed in order to process the obtained data for predicting the temperature of visible heat source. Color temperature correlation expressed through linear regression is analysed with other methods, and it is observed that RGB outperforms the HSI model. The prediction is improved by image segmentation, and so more equations are functioned out using IG-MM to improve the applicability of model. As the flame comprises various zones, it provides non-linear characteristics thereby with the support of neural network better outcomes has obtained than existing approaches. Accordingly, the temperature prediction using CSAtt-CWAN has enhanced the performance and so the proposed OptiA-DL model exhibits greater potential for temperature measurement close to actual temperature. Besides, the results showed that the error values in terms of MSE, MAE and RMSE are reduced and so the accuracy of temperature measurement is improved. This is due to the application of WHOA in CSAtt-CWAN that supports to minimize the loss and improve the accurate prediction of temperature. The red color in image has utilized to obtain the correlation of actual temperature and pixel intensity. The temperature varies rendering to the flame color, as the color is darker it resembles higher temperature. Moreover, from the experimental outcomes, it is stated that the proposed OptiA-DL model seems to be superior to prevailing approaches for measuring the temperature of several visible heat sources as molten metal, boiler, furnace and so on.

5. Conclusion

A novel OptiA-DL strategy is contributed in this paper to determine the temperature of visible heat sources. Various phases, such as image acquisition, image pre-processing, image segmentation, feature extraction, and temperature measurement, are encompassed in the OptiA-DL strategy. The new guided co-operative trilateral filter (GCTF) used in the OptiA-DL strategy supports smoothening the image and evading the reflections. The Kepler optimization algorithm (KoA) adopted in the Gaussian mixture model assists in successfully segmenting the image into diverse portions. The improved temperature prediction has been established through a compact split attention-based convolutional waderhunt autoencoder network (CSAtt-CWAN) model, where the hyper-parameters

are altered by means of waderhunt optimization algorithm (WHOA). Subsequently, the performance of the proposed OptiA-DL strategy is related to prevailing methods, including LSTM, Bi-LSTM, ANN, and CNN, to compute the efficacy of temperature measurement. In contrast to prevailing methods, the OptiA-DL strategy has accomplished better MAE of 1.012, MSE of 0.076 and RMSE of 0.011, respectively. Even accomplishing better performance in different error measures, the proposed OptiA-DL still requires extending the temperature measurement performance. Additional enquiry can be essential to understand the model's reliability in dissimilar datasets.

Conflicts of interest

The authors declare no conflict of interest.

Author contributions

Conceptualization, Sanket and Ajit Kumar; methodology, Sanket and Ajit Kumar; software, Sanket; validation, Sanket; formal analysis, Sanket and Ajit Kumar; investigation, Sanket; resources, Sanket; data curation, Sanket; writing-original draft preparation, Sanket; writing-review and editing, Sanket and Ajit Kumar; visualization, Sanket; supervision, Sanket; project administration, Sanket and Ajit Kumar; funding acquisition, Sanket. All authors have read and approved the final manuscript.

Acknowledgments

We wish to thank the School of Electronics Engineering and School of Computer Science Engineering and Information Systems of VIT University as well as faculties, management of VIT for their support and encouragement.

References

[1] Z. Wang, T. Zhang, and X. Huang, "Predicting real-time fire heat release rate by flame images and deep learning", In: *Proc of the Combustion Institute*, Vol. 39, No. 3, pp. 4115-4123, 2023.

[2] J. Huang, H. Liu, and W. Cai, "Online in situ prediction of 3-D flame evolution from its history 2-D projections via deep learning", *Journal of Fluid Mechanics*, Vol. 875, p. R2, 2019.

[3] D. Pan, Z. Jiang, C. Xu, and W. Gui, "Polymorphic temperature measurement method of molten iron after skimmer in ironmaking process", *IEEE Transactions on Instrumentation and Measurement*, Vol. 71, pp. 1-11, 2022.

[4] K. Grujić, "A Review of Thermal Spectral Imaging Methods for Monitoring High-Temperature Molten Material Streams", *Sensors*, Vol. 23, No. 3, p. 1130, 2023.

[5] D. Holler, R. Vaghetto, and Y. Hassan, "High-resolution wall temperature measurements with distributed fiber optic sensors", *International Journal of Thermal Sciences*, Vol. 145, p. 106042, 2019.

[6] D. I. Gillespie, A. W. Hamilton, E. J. M. Kay, B. Neilson, R. C. Atkinson, I. Andonovic, and C. Tachtatzis, "Non-destructive identification of fibre orientation in multi-ply biaxial laminates using contact temperature sensors", *Sensors*, Vol. 20, No. 14, p. 3865, 2020.

[7] L. J. Nayak and G. G. Roy, "Thermocouple temperature measurement during high speed electron beam welding of SS 304", *Optik*, Vol. 201, p. 163538, 2020.

[8] F. Shih, C. Tsou, and W. Fang, "A monolithic micromachined thermocouple probe with electroplating nickel for micro-LED inspection", *Journal of Microelectromechanical Systems*, Vol. 30, No. 6, pp. 864-875, 2021.

[9] Q. Liu, B. Zhou, R. Cheng, J. Zhang, R. Zhao, M. Dai, X. Zhao, and Y. Wang, "Online monitoring instantaneous 2D temperature distributions in a furnace using acoustic tomography based on frequency division multiplexing", *Case Studies in Thermal Engineering*, pp. 103176, 2023.

[10] C. T. Salinas, Y. Pu, C. Lou, and D. B. D. Santos, "Experiments for combustion temperature measurements in a sugarcane bagasse large-scale boiler furnace", *Applied Thermal Engineering*, Vol. 175, p. 115433, 2020.

[11] S. S. Mane and R. T. Patil, "Temperature Measurement of visible heat sources using neural network", *An International Journal (ELELIJ)*, Vol. 4, No. 2, 2015.

[12] J. Kosir, D. Vella, and M. Jezersek, "Non-contact monitoring of the depth temperature profile for medical laser scanning technologies", *Scientific reports*, Vol. 10, No. 1, p. 20242, 2020.

[13] Y. Yang and X. Lee, "Four-band thermal mosaicking: A new method to process infrared thermal imagery of urban landscapes from UAV flights", *Remote Sensing*, Vol. 11, No. 11, p. 1365, 2019.

[14] Z. Sun, M. Cui, M. Nour, X. Li, D. Hung, and M. Xu, "Study of flash boiling combustion with different fuel injection timings in an optical engine using digital image processing diagnostics", *Fuel*, Vol. 284, p. 119078, 2021.

[15] M. Nehir, C. Frank, S. Abmann, and E. P.

Achterberg, “Improving optical measurements: non-linearity compensation of compact charge-coupled device (CCD) spectrometers”, *Sensors*, Vol. 19, No. 12, p. 2833, 2019.

[16] N. Inada, N. Fukuda, T. Hayashi, and S. Uchiyama, “Temperature imaging using a cationic linear fluorescent polymeric thermometer and fluorescence lifetime imaging microscopy”, *Nature Protocols*, Vol. 14, No. 4, pp. 1293-1321, 2019.

[17] Y. Wang, Y. Yu, X. Zhu, and Z. Zhang, “Pattern recognition for measuring the flame stability of gas-fired combustion based on the image processing technology”, *Fuel*, Vol. 270, p. 117486, 2020.

[18] J. Pan, J. A. Libera, N. H. Paulson, and M. Stan, “Flame stability analysis of flame spray pyrolysis by artificial intelligence”, *The International Journal of Advanced Manufacturing Technology*, Vol. 114, No. 7-8, pp. 2215-2228, 2021.

[19] A. S. R. Bishoyi, R. Goel, V. Batra, K. T. Jacob, S. Agarwal, M. Sriram, C. S. Abhijit, and G. Rohith, “A Deep Learning approach for fire object detection in Autonomous vehicles”, *In Journal of Physics: Conference Series*, Vol. 2466, No. 1, p. 012031, 2023 IOP Publishing,

[20] M. Dai, B. Zhou, J. Zhang, R. Cheng, Q. Liu, R. Zhao, B. Wang, and B. Gao, “3-D soot temperature and volume fraction reconstruction of afterburner flame via deep learning algorithms”, *Combustion and Flame* Vol. 252, p. 112743, 2023.

[21] M. C. Catalbas and M. B. Kobav, “Measurement of correlated color temperature from RGB images by deep regression model”, *Measurement*, Vol. 195, p. 111053, 2022.

[22] G. Agrawal, R. Mishra, A. Ransingh, and S. Chakravarty, “Flame Temperature Prediction Using Machine Learning Model”, In: *Proc. of 2020 IEEE India Council International Subsections Conference (INDISCON)*, pp. 157-162, 2020.

[23] S. Sawada, D. Okada, N. Nakatsuka, K. Tainaka, T. Hori, J. Hayashi, and F. Akamatsu, “Time-series temperature measurement during combustion of volatile matter and coal char of a single pulverized coal particle via magnified two-color pyrometry with blue backlit imaging”, *Energy & Fuels*, Vol. 34, No. 10, pp. 12918-12925, 2020.

[24] L. Shan, H. Huang, B. Hong, J. Zhao, D. Wang, and M. Kong, “Temperature measurement method of flame image fusion with different exposures”, *Energies*, Vol. 13, No. 6, p. 1487, 2020.

[25] W. Yan, Z. Hu, K. Li, X. Xing, H. Gong, B. Yu, and H. Zhou, “Numerical Simultaneous Determination of Non-Uniform Soot Temperature and Volume Fraction from Visible Flame Images”, *Energies*, Vol. 15, No. 8, p. 2770, 2022.